Published in Engineering Fracture Mechanics, 2008, 75(16), 4774-4792
doi:10.1016/j.compositesa.2011.12.016

Cohesive Zone Length in Numerical Simulations of Composite Delamination

Paul W. Harper and Stephen R. Hallett

Advanced Composites Centre for Innovation and Science
University of Bristol
Queen's Building, University Walk, Bristol, BS8 1TR, UK

Abstract:

Accurate analysis of composite delamination using interface elements relies on having sufficient elements within a softening region known as the cohesive zone ahead of a crack tip. The present study highlights the limitations of existing formulae used to predict numerical cohesive zone length and demonstrates modifications necessary for improved accuracy. Clarification is also provided regarding the minimum number of interface elements within the cohesive zone. Finally, appropriate values of numerical interfacial strength are examined. The results presented will aid the application of mesh design techniques that both preserve numerical accuracy, whilst minimising computational expense.

Keywords: Composites; Delamination; Interface Fracture; Finite Element Analysis; Cohesive Zone Modelling

Published in Engineering Fracture Mechanics, 2008, 75(16), 4774-4792
doi:10.1016/j.compositesa.2011.12.016

Nomenclature

Interface Element Properties:

G = Strain Energy Release Rate (N/mm)

G_C = Critical Strain Energy Release Rate (N/mm)

K = Interface Element Stiffness prior to damage initiation (N/mm^3)

σ = Interface Element Stress (MPa)

σ_{max} = Interfacial Strength (MPa)

δ = Interface Element Relative Displacement (mm)

δ_e = Interface Element Relative Displacement at damage initiation (mm)

δ_f = Interface Element Relative Displacement at final failure (mm)

Laminate Material Properties:

E_{11}, E_{22}, E_{11} = Young's Moduli (MPa)

G_{12}, G_{13}, G_{23} = Shear Moduli (MPa)

ν_{12}, ν_{13}, ν_{23} = Poisson's Ratios

where subscripts 1, 2 and 3 denote the principal material axes

Laminate Geometric Properties

h = Laminate Half Thickness (mm)

B = Laminate Width (mm)

X = Specimen Length (mm)

a = Crack Length (mm)

a_0 = Initial Crack Length prior to crack propagation (mm)

I = Second Moment of Area (mm^4)

Other:

P = Load (N)

Δ = Cantilever Tip Displacement (mm)

l_{ch} = Characteristic Cohesive Zone Length in an infinite body (mm)

$l_{ch,slender}$ = Characteristic Cohesive Zone Length in a slender body (mm)

$E^{'}$ = Equivalent Elastic Modulus used in the characteristic length equation for orthotropic materials (MPa)

L_{CZ} = Numerical Cohesive Zone Length (mm)

$L_{CZ,f}$ = Fully Developed Numerical Cohesive Zone Length (mm)

N_{el} = Number of elements within the numerical cohesive zone

L_{el} = Element Length (mm)

Where applicable, subscripts *I*, *II* and *m* are used to denote properties under mode I, mode II and mixed mode loading respectively.

Published in Engineering Fracture Mechanics, 2008, 75(16), 4774-4792
doi:10.1016/j.compositesa.2011.12.016

1. Introduction and Motivation

Interface elements are specialised finite elements used to simulate crack initiation and propagation in numerical models. Over recent years, they have become increasingly used for modelling composites, particularly in relation to delamination [1,2,3,4,5,6,7] and adhesive bond-line failure [8,9,10,11]. Compared with alternative analysis techniques such as the Virtual Crack Closure Technique (VCCT), they offer the advantages of encompassing both crack initiation and crack propagation and the ability to model multiple crack paths, without the need for computationally expensive crack-path following algorithms. In addition, they do not require the direction of crack propagation to be known a priori, and cracks have the potential to propagate along any path where interface elements are placed [12]. Figure 1 demonstrates a typical simulation of composite delamination in a mode I Double Cantilever Beam (DCB).

(Insert figure 1 showing interface element representation)

An interface element's behaviour is governed by a traction-displacement curve, relating element stress (traction) to mode I (opening) and mode II (shear) nodal displacements. Although a variety of geometric shapes have been used for this traction-displacement curve, a bi-linear form is commonly implemented for modelling composite delamination (see figure 2). This consists of the following main features:

1. An initial elastic region until reaching a maximum stress (σ_{max}), which represents the interfacial strength.
2. A subsequent softening region until zero stress is reached and element failure

occurs.

3. The total area enclosed by the curve is equal to the fracture toughness of the material.

(Insert figure 2 showing bi-linear traction displacement curve and main features)

Ahead of a numerical crack tip, we can define a region known as the cohesive zone, in which elements experience irreversible deformation (i.e. region δ_e - δ_f on the traction displacement response shown in figure 2). Figure 3 illustrates the development of this zone, using the simple example of a mode I DCB specimen subject to a linearly increasing tip displacement. As displacement initially increases, the interface element adjacent to the crack tip rapidly reaches its maximum interfacial strength and moves onto the softening region of the traction-displacement response. As tip displacement increases further, adjacent elements also undergo irreversible deformation, allowing a cohesive zone length, L_{CZ}, to be defined, over which stress increases up to the maximum interfacial strength some distance ahead of the crack tip. The length of the cohesive zone reaches a maximum, $L_{CZ,f}$, at the point where the crack tip interface element fails completely and the crack starts to propagate.

(Insert figure 3 showing cohesive zone development in a mode I DCB)

It is important to draw a clear distinction between the true physical cohesive zone length, defined as the length over which irreversible damage processes occur ahead of a crack tip and the numerical cohesive zone length, over which interface elements lie on the softening part of their traction-displacement response. For an accurate numerical

representation of the physical cohesive zone, the shape of the traction-displacement curve must reflect the stress distribution associated with damage mechanisms occurring ahead of the physical crack tip [13]. However, this stress distribution is very difficult to measure experimentally and, if only a global analysis of the structure's load-displacement response is required, results are relatively insensitive to the exact shape of the traction-displacement curve, provided that the correct interfacial strength and fracture toughness are applied [12]. This explains why the bi-linear traction-displacement curve, which is geometrically the most simple form to implement, has become commonly used for delamination analyses [5,6,7]. Furthermore, once a crack has initiated in a structure and a cohesive zone exists, results are relatively insensitive to the exact value of interfacial strength and only the fracture toughness value is of critical importance [14].

In order to conduct an accurate delamination analysis, the mesh must be sufficiently fine to ensure that enough interface elements exist within the cohesive zone length at the point of crack propagation. However, for large structural models, it is also important to avoid the computational expense of an excessively fine mesh. Therefore, mesh optimisation relies on accurate values for both cohesive zone length and the minimum number of interface elements required within this. An accurate prediction of cohesive zone length is also required in interface element fatigue degradation laws [15].

When pioneering the use of cohesive zone models in finite element analyses of crack formation and growth in concretes, Hillerborg et al. [16] presented a characteristic length parameter (l_{ch}) for isotropic materials, which is a material property given by the following equation:

Published in Engineering Fracture Mechanics, 2008, 75(16), 4774-4792
doi:10.1016/j.compositesa.2011.12.016

$$l_{ch} = E\frac{G_C}{(\sigma_{max})^2} \quad (1)$$

For the analysis of crack growth in orthotropic materials, modified versions of equation (1) have been developed [12, 17], which for mode I and mode II loading are given by:

$$l_{ch,I} = E_I^{'}\frac{G_{IC}}{(\sigma_{I,max})^2} \quad (2a)$$

$$l_{ch,II} = E_{II}^{'}\frac{G_{IIC}}{(\sigma_{II,max})^2} \quad (2b)$$

where *E'* is an equivalent elastic modulus (MPa) for orthotropic materials, whose value depends on the material's longitudinal modulus, transverse modulus, shear modulus, depth and whether plane stress or plane strain conditions exist [17]. This replaces the isotropic elastic modulus in equation (1). The procedure for calculating *E'* is provided in Appendix A.

Values equal to or close to the characteristic length have since been suggested by several authors [12,14,17] for predicting the maximum numerical cohesive zone length, $L_{CZ,f}$, and hence, required mesh density, in finite element analyses. The present study highlights that the characteristic length can significantly over-predict the maximum numerical cohesive zone length. This finding is consistent with existing analytical solutions for cohesive zone length. For example, Planas and Elices [18] have compared fully developed cohesive zone lengths in remotely loaded, isotropic, infinite bodies resulting from rectilinear, linear and exponential softening traction-displacement laws. They found the cohesive zone length to be given by $(\pi/8)\ l_{ch}$, $0.731\ l_{ch}$ and $2.92\ l_{ch}$ for rectilinear, linear

and exponential softening laws respectively. This strong dependence of cohesive zone length on traction-displacement curve shape has also been shown by Smith [19], who developed closed form cohesive zone length solutions for a range of power law curves. One of these curves gave a close approximation of the linear softening law and similar results to those of Planas and Elices were gained.

There are several significant differences between these analytical solutions for cohesive zone length and the present numerical study. All the examples quoted are based on the development of cracks in isotropic materials, but as highlighted by Yang et al. [12,17] and shown by equations (2a) and (2b), when analysing cohesive zone length in orthotropic materials, the elastic modulus in the characteristic length equation becomes a function of the material's longitudinal modulus, transverse modulus, shear modulus, depth and plane stress or plane strain conditions. In Turon et al.'s previous study [14], the value of E' was assumed equal to the transverse modulus when predicting cohesive zone length. The present study highlights the importance of including the additional parameters listed above in the calculation of cohesive zone length for orthotropic materials.

Furthermore, the analytical traction-displacement curves discussed above prescribe maximum cohesive traction at zero crack opening displacement. However, when implementing a cohesive zone law in a numerical model, it is necessary to have an initial rising part of the traction-displacement curve, which is generally taken as linear to simulate the elastic response of the interface until the point of damage initiation.

Finally, the above analytical solutions are for infinite bodies, where material depth has no influence on cohesive zone length. For analysis of composite delamination and

bond-line failure, it is critical that the effects of specimen thickness on cohesive zone length are studied, due to the slender nature of typical laminates. Williams and Hadavinia [20] conducted an analytical investigation of cohesive zone models applied to a slender DCB specimen, incorporating a range of traction-displacement laws. Their work was motivated by developing analytical solutions for the equivalent crack length in a purely elastic material, as opposed to the length of the cohesive zone. Based on previous studies of crack bridging models [21,22], Cox and Yang proposed modified forms of the characteristic length equations for infinite bodies (equations (2a) and (2b)), which they suggest should be used for estimating cohesive zone length in slender laminates, with centred cracks, under mode I and mode II loading respectively [12]:

$$l_{ch,slender,I} = \left(E_I' \frac{G_{IC}}{(\sigma_{I,max})^2} \right)^{\frac{1}{4}} h^{\frac{3}{4}} \tag{3a}$$

$$l_{ch,slender,II} = \sqrt{\left(E_{II,slender}' \frac{G_{IIC}}{(\sigma_{II,max})^2} \right) h} \tag{3b}$$

where h is the laminate half-thickness and $E'_{II,slender}$ is a mode II equivalent elastic modulus for a slender body, which takes a different form to that used in equation (2b) (see Appendix A). The mode I equivalent elastic modulus takes the same form as that used in equation (2a). These formulae are based on the assumption that the characteristic length parameter, l_{ch}, provides an accurate prediction of cohesive zone length in an infinite body, which as previously discussed, is not necessarily the case. In addition, no guidance is provided concerning what constitutes a slender laminate.

No numerical studies have been presented to validate the accuracy of equations (2) and (3) across a range of material properties, structural geometries and load conditions. The present paper addresses this need by investigating whether the functional forms of these equations are applicable to numerical cohesive zone lengths and under what conditions each formula provides the greatest level of accuracy. This is of significant importance, both in mesh optimisation techniques for interface element models, and the development of fatigue laws based on the degradation of interface elements within the cohesive zone.

With respect to the minimum number of interface elements required within the cohesive zone for an accurate failure analysis, recommendations in the literature show a wide variation, ranging from two to more than ten [14]. Recent composite delamination analyses using interface elements have suggested that 2-3 elements are sufficient for mode I load cases [14,23]. This study provides a more detailed investigation, with respect to the development of the numerical cohesive zone, for mode I, mode II and mixed mode load cases.

A final aim of the paper is to examine appropriate values of interfacial strength for modelling composite delamination. This is motivated by a technique recently demonstrated by Turon et al. [14] for reducing the required mesh density, by using a reduction in numerical interfacial strength to increase the cohesive zone length. Such a method is very beneficial for delamination analyses involving typical composite epoxy resins, which can have cohesive zone lengths of less than 1mm if a realistic interfacial strength is applied. As discussed above, a reduced numerical interfacial strength is allowable due to evidence that once a crack has initiated, results are relatively insensitive to the exact value of this

parameter, provided that an accurate fracture toughness (area enclosed by the traction-displacement curve) is maintained. However, a previous investigation by Blackman et al. [9] has shown that excessively low values of interfacial strength can result in an inaccurate load-displacement analysis. In this case, a polynomial traction-displacement law was implemented, in which the interface element stiffness varies prior to reaching the maximum interfacial strength (i.e. in the region 0 - δ_e shown on figure 2). Whilst the present study uses a bi-linear law, in which interface element stiffness remains constant in this region, the effects of reducing interfacial strength appear consistent with those previously highlighted by Blackman et al. This suggests that limits should be set on allowable reductions in interfacial strength as a means of reducing the required mesh density. As for standard mesh design techniques, Turon et al.'s procedure [14] relies on accurate values of numerical cohesive zone length and the minimum number of interface elements required within this.

2. Interface Element Formulation

The interface elements used for this study take the form of solid hexahedral elements with a small initial thickness and are governed by a bi-linear constitutive law. This was developed from a discrete interface element formulation, which has been successfully implemented to model both matrix cracking and delamination within notched composites using the explicit finite element code LS-DYNA [7]. Full details of the formulation are given in this previous study and so only a brief overview is now provided.

The formulation can be illustrated in a single three-dimensional map, as used by several previous authors [5,6,7,24], by representing the normal opening mode (mode I) on the 0 - σ - δ_{normal} plane, and the transverse shear mode (mode II) on the 0 - σ - δ_{shear} plane,

Published in Engineering Fracture Mechanics, 2008, 75(16), 4774-4792
doi:10.1016/j.compositesa.2011.12.016

as shown in figure 4. The triangles *0* - $\sigma_{I,max}$ - $\delta_{I,f}$ and *0* - $\sigma_{II,max}$ - $\delta_{II,f}$ are the bi-linear responses in the pure opening and pure shear modes respectively. Any point on the *0* - δ_{normal} - δ_{shear} plane represents a mixed-mode relative displacement.

(Insert figure 4 showing the mixed mode 3-D map)

The mixed mode damage onset displacement, $\delta_{m,e}$, and interfacial strength, $\sigma_{m,max}$, are calculated using a quadratic damage onset criterion:

$$\sqrt{\left(\frac{max(\sigma_I,0)}{\sigma_{I,max}}\right)^2+\left(\frac{\sigma_{II}}{\sigma_{II,max}}\right)^2}=1 \qquad (4)$$

The mixed mode failure displacement corresponding to complete decohesion is calculated using the following power law failure criterion:

$$\left(\frac{G_I}{G_{IC}}\right)^{\alpha}+\left(\frac{G_{II}}{G_{IIC}}\right)^{\alpha}=1 \qquad (5)$$

where $\alpha \in (1.0 \sim 2.0)$ is an empirical parameter derived from mixed-mode tests, G_{IC} and G_{IIC} are critical energy release rates for pure mode I (opening) and pure mode II (shear) respectively. Equation (5) allows the fully debonded locus, represented by the relative displacement corresponding to complete interface failure, $\delta_{m,f}$, to be determined (see figure 4).

3. Benchmark Applications

The baseline specimen geometry, laminate properties and interfacial properties used for the present investigation are as specified in figure 5 and table 1. These are based on

experimental data using HTA/6376C [25], for which numerous researchers have previously conducted numerical delamination analyses under both static [26,27] and fatigue loading [15,28]. The analyses presented here have been conducted under mode I, mode II and mixed mode loading, using the DCB, 3 Point End Notched Flexure (3ENF) and Fixed Ratio Mixed Mode (FRMM) specimens respectively. The details of each model, including boundary conditions and properties of the numerical interface are shown in figure 6. It should be noted that the mode II interfacial strength of 60MPa is significantly higher than that of 30MPa [15,28] and 40MPa [26,27] applied by previous authors. As discussed in section 4.3, this was necessary to perform an accurate quasi-static load-displacement analysis of the 3ENF and FRMM specimens. Numerical results have been compared with both experimental results and corrected beam theory results (see appendix B) for the mode I and mode II load cases. Since no experimental data was available in the open literature for the mixed mode load case, only a comparison with corrected beam theory, with α set to 1 in equation (5), has been made.

(Insert figure 5, table 1 and figure 6)

4. Results

4.1 Minimum Number of Interface Elements required within the cohesive zone

As shown by figure 7, for the mode I DCB, the numerical cohesive zone length at the point of initial crack propagation (i.e. the crack tip interface element reaching zero traction) was measured as 1.2mm for an element length, L_{el}, of 0.125mm. Plotting a trendline through results for element lengths of 0.25mm and 0.5mm also provides close

agreement with this value.

(Insert figure 7)

Referring to figure 8(a), it is evident that all of these element lengths enable an accurate analysis of the global load-displacement response. However, the smoothness of the solution in the propagation regime decreases with increasing element length caused by dynamic effects as each interface element fails, due to the increasing fracture energy released by larger elements. A global damping factor of 5 was applied in all analyses to remove high frequency oscillations whilst maintaining accurate results. With element length increased to 1mm, it is no longer possible to capture the cohesive zone stress distribution and the accuracy of the analysis decreases. Results become progressively worse with further reductions in mesh density (see figure 8(b)).

(Insert figure 8)

In the present study, the number of interface elements within the cohesive zone, $N_{el,}$ is defined as:

$$N_{el} = \frac{L_{CZ,f}}{L_{el}} \qquad (6)$$

where $L_{CZ,f}$ is the length of the cohesive zone at the point of first element failure, when using a fine mesh that enables the cohesive zone stress distribution to be accurately captured. In the present analyses, $L_{CZ,f}$ was measured using a 0.125mm element length for the DCB and FRMM specimens and a 0.25mm element length for the 3ENF specimen. The longer element length used for the 3ENF specimen was possible due to the greater length of

the cohesive zone.

The trends discussed above suggest that the minimum value of N_{el} required to gain an accurate analysis of the mode I DCB specimen lies somewhere between 1.2 and 2.4, the values calculated for element lengths of 1mm and 0.5mm respectively. This appears consistent with previous mode I studies [14,23], which have suggested that at least 2 elements are required within the cohesive zone for an accurate global load-displacement analysis.

Similar results are exhibited for the 3 point ENF and FRMM specimens (figures 9 to 12). In the case of the 3 point ENF, which has a numerical cohesive zone length of 4.1mm (see figure 9), there is a significant reduction in the accuracy of results when increasing element length from 1.5mm to 2mm. For an element length of 1.5mm, results show close agreement with those obtained using finer meshes. When element length is increased to 2mm, the model fails to accurately capture the point of propagation and there are significant oscillations present in the propagation regime. This suggests that the minimum value of N_{el} for an accurate analysis lies somewhere between 2.05 and 2.73. (N.B. Results for the finest mesh used for the 3ENF, with an element length of 0.25mm, have not been displayed on figures 9 and 10 because, due to the long cohesive zone length, they show no significant variation from those for an element length of 0.5mm).

For the FRMM specimen, which has a numerical cohesive zone length of 1.5mm, analysis accuracy deteriorates when element length is increased from 0.5mm to 1mm. This indicates that the minimum value of N_{el} lies between 1.5 and 3.

(Insert figures 9 to 12)

Although further work remains to precisely define a minimum required N_{el} for accurate numerical analyses under various mode ratios, a conservative approach would be to require that $N_{el} \geq 3$. This will ensure that the cohesive zone stress distribution at the point of first element failure is correctly captured, hence preventing delayed propagation onset.

4.2 Cohesive Zone Length

Since equations for estimating cohesive zone length are dependent on E', G_C, σ_{max} and h (see equations (2) and (3)), their effects on the fully developed numerical cohesive zone length, $L_{CZ,f}$, have been investigated. Figure 13 shows the effects on $L_{CZ,f}$ of independently varying these parameters for the benchmark HTA6376/C mode I DCB model, using a consistent element length of 0.125mm. (N.B. As shown in Appendix A, E' is influenced by E_{11}, E_{33} and G_{13}, therefore, each of these parameters has been independently varied). Due to the uncertainties surrounding the accuracy of existing predictive formulae highlighted in the introduction, a scaling factor, M, has been applied to equations (2) and (3), to try and identify the best fit to numerical results.

When comparing the numerical results with equations (2a) and (3a) (i.e. the characteristic cohesive zone lengths, $l_{ch,I}$ and $l_{ch,slender,I}$, in infinite and slender bodies respectively), it was apparent that both formulae significantly over-predict the numerical cohesive zone length. As a result, using these formulae for mesh design risks the application of a mesh that is too coarse to accurately model failure. It was identified that applying $M = 0.5$ to equation (3a), which accounts for the influence of specimen depth, provides a reasonable and generally conservative correlation with the numerical results

across most of the parameter ranges investigated. In cases where material properties result in a very short cohesive zone length (e.g. high interfacial strength, low shear modulus, low transverse modulus), equation (2a), which takes no account of structural depth, begins to exhibit a closer match to the numerical results. Again, it is necessary to use $M = 0.5$ in order to gain a close match with the numerical results. It is apparent that this value falls between the analytical solutions for cohesive zone lengths in infinite bodies of $M = \pi/8$ and $M = 0.731$, for rectilinear and linear softening traction-displacement laws respectively [18]. Equations (2a) and (3a), with a scaling factor of $M = 0.5$ applied, have been plotted on figure 13 to highlight the trends discussed.

(Insert figure 13)

Very similar observations can be made for the mode II cohesive zone length results shown in figure 14, for an element length of 0.25mm. Again, equation (3b), which accounts for structural depth, generally provides the best correlation with numerical results, but it is necessary to apply $M = 0.5$ to gain a close match. Previous work by Massabo and Cox [22] has shown that the equivalent mode II modulus in the characteristic length equation for slender bodies, $E'_{II,slender}$, takes the same value as the longitudinal modulus, E_{11}, and is influenced by no other elastic moduli. However, the cohesive zone length in the 3ENF specimen is seen to increase from a value of 3mm for a shear modulus, G_{13}, of 1000MPa to 4.3mm for a shear modulus, G_{13}, of 7000MPa. Therefore, whilst the influence of shear modulus is relatively weak compared to that of longitudinal modulus, it cannot be neglected. This highlights the difficulty in drawing a clear distinction between what constitutes a slender or infinite body. Relative to the mode I load case, the cohesive zone

lengths for mode II are significantly longer. As suggested by previous authors [12], this highlights that for typical composite material properties, it will generally be the mode I cohesive zone length that dictates the minimum mesh density.

(Insert figure 14)

In order to investigate the accuracy of equations (2) and (3) in situations where the structural depth has a less significant influence, an additional mode I DCB model was created, using the specimen geometry and material properties shown in table 2. This is based on data provided in reference [14] for a T300/977-2 specimen, which has a significantly increased mode I fracture toughness, G_{IC} (+74%), interfacial strength, $\sigma_{I,max}$ (+200%), specimen depth, h (+32%), initial crack length, a_0 (+57%), and longitudinal modulus, E_{11} (+25%), relative to the HTA/6376C specimen. A consistent element length of 0.125mm was again used.

(Insert table 2)

Figure 15 highlights that for these material properties, the specimen depth has a much less significant influence across the range of parameters investigated and equation (2a) frequently gives a more accurate prediction of numerical cohesive zone length than equation (3a). Again, it is necessary to apply $M = 0.5$ to gain a close match to the numerical results. Only for cases where the variation of a material property significantly extends the cohesive zone length, such as reduced interfacial strength or increased fracture toughness, does equation (3a) provide the best correlation. It is always the minimum of the two analytical values, provided by equations (2a) and (3a) respectively, which provides the

closest match to numerical results.

(Insert figure 15)

The cohesive zone length results for both the mode I and mode II load cases suggest that a reasonable match to the numerical results is always obtained by applying $M = 0.5$ to the minimum value from equations (2) and (3). Further work remains to investigate appropriate values of M for alternative traction-displacement laws and for a wider range of crack lengths and structural geometries.

Combining these results with those discussed in section 4.1, the proposed mesh design strategy for a general mixed mode load case, when using a bi-linear traction-displacement law, is as follows:

i) Predict the minimum possible length of the fully developed cohesive zone, $L_{CZ,f,predicted}$, using the formula,

$$L_{CZ,f,predicted} = 0.5\left[min\left(Eqn.2(a), 2(b), 3(a), 3(b)\right)\right] \qquad (7)$$

Based on the cohesive zone results presented in figures 13 to 15, the only case where this formula risks providing a significant over-prediction of cohesive zone length is when the transverse modulus, E_{33}, has a value above 12,000MPa. This is apparent from figure 15, where the numerical cohesive zone length for the T300/977-2 DCB model shows a maximum variation of 30% below that predicted by equation 3(a) with a scaling factor of $M = 0.5$ applied.

ii) Divide this result by 3 to calculate the maximum allowable element length, $L_{el,max}$, in order to ensure that at least 3 interface elements are present within the fully developed

cohesive zone:

$$L_{el,max} = \frac{L_{CZ,f,predicted}}{3} \quad (8)$$

4.3 Effects of varying Numerical Interfacial Strength

Figures 16 to 18 show the effects of varying mode I and mode II interfacial strength on the load-displacement analyses of the benchmark DCB, 3ENF and FRMM specimens. For each specimen, results are presented in the following forms:

i) Using a fine mesh, which enables the cohesive zone stress distribution to be accurately captured for all values of numerical strength investigated. The fully developed cohesive zone length, $L_{CZ,f}$, for each value of interfacial strength is also shown so that the accuracy of the analyses can be related to this parameter.

ii) Using a coarse mesh, where the number of elements within the cohesive zone is initially less than the minimum required value, when applying the baseline interfacial strength (see section 4.1). This enables allowable reductions in interfacial strength to be investigated, when using this technique to reduce the minimum required mesh density, as originally proposed by Turon et al. [14].

In figure 16(a), mode I interfacial strength is reduced from 45MPa (15MPa above the baseline value) to 5MPa for the DCB specimen, using a fine mesh with an element length of 0.125mm. Between 45MPa and 30MPa there is no significant change in the accuracy of the numerical analysis and both load-displacement curves show close agreement with corrected beam theory. From 30MPa to 10MPa, there is a gradual loss of stiffness in the elastic loading regime prior to crack propagation, but this is reasonably

small in magnitude and does not produce a large deterioration in analysis accuracy. When the numerical interfacial strength is decreased from 10MPa to 5MPa and the cohesive zone length increases from 3.25mm to 6mm, a much larger deterioration in stiffness occurs and the point of crack propagation is significantly delayed. Figure 16(b) shows the effects of reducing mode I interfacial strength for a coarse mesh of 1mm element length, which is unable to accurately capture the cohesive zone distribution at the point of first element failure when using the baseline value of 30MPa (see figure 8(b)). As interfacial strength is reduced, the same trends as those discussed for the fine mesh regarding loss of stiffness in the elastic regime are apparent. However, significant improvements in analysis accuracy in the propagation regime are gained due to an increased number of elements within the cohesive zone at the point of first element failure.

(Insert figure 16)

Figure 17(a) shows the effects of varying interfacial strength for the 3ENF specimen, using a fine mesh with an element length of 0.25mm. It is evident that for a mode II interfacial strength of 30MPa, as applied by previous authors [15,28], the analysis cannot accurately capture the peak load prior to crack propagation. This is due to a significant loss of stiffness during the elastic loading regime. However, with interfacial strength increased to a more realistic value of 60MPa, a much closer match to the corrected beam theory solution is obtained. No significant further improvement is gained by increasing interfacial strength to 90MPa. This justifies the value of 60MPa selected for the numerical mode II interfacial strength in the baseline model. The poor results gained using lower values of interfacial strength are believed to be due to the very long numerical

cohesive zone lengths (10.5mm for 30MPa and 20.25mm for 15MPa) and hence significant softening ahead of the crack tip. Figure 17(b) shows the effects of reducing interfacial strength using a coarse mesh with an element length of 2mm. This element length is greater than that of 1mm used for the DCB due to the longer cohesive zone length resulting from the baseline material properties. This means that for the 3ENF model, it is only when element length is increased from 1.5mm to 2mm that there becomes an insufficient number of elements within the cohesive zone to accurately capture the point of crack propagation (see figure 10). As for the DCB, reduced interfacial strength increases the accuracy of the analysis in the propagation regime. However, comparison with figure 17(a) shows that the initial point of crack propagation for a fine mesh cannot be regained. This is likely to be due to the coarseness of the mesh combined with the very sudden nature of crack propagation in the 3ENF specimen.

(Insert figure 17)

Figure 18(a) shows the effects of reducing mode I and mode II interfacial strengths in equal proportions below their baseline values for the FRMM specimen, when using a fine mesh with an element length of 0.125mm. The cohesive zone lengths exhibited for each combination of mode I and mode II interfacial strength appear to be dictated mainly by the mode I value. This explains why, similar to the mode I DCB, a significant loss in stiffness within the elastic regime only occurs when mode I interfacial strength is reduced below 10MPa and the cohesive zone length exceeds approximately 5mm. Figure 18(b) shows the effects of reducing mode I and mode II interfacial strengths, for a coarse mesh of 1mm element length, which is unable to capture the cohesive zone distribution at the point

of first element failure when using the baseline values of 30MPa and 60MPa respectively (see figure 12). Similar to results for the mode I DCB, significant improvements in analysis accuracy within the propagation regime are obtainable with reduced interfacial strength but at the expense of reduced stiffness in the elastic regime.

(Insert figure 18)

The above findings indicate that care must be taken when reducing interfacial strength as a means of reducing the required mesh density in numerical models. For typical carbon epoxy properties, a very short mode I cohesive zone length exists, allowing significant reductions in mode I interfacial strength, without affecting the accuracy of global load-displacement analyses. However, mode II cohesive zone lengths are generally much longer, and similar mode II interfacial strength reductions can result in significant inaccuracies. Further investigation is required to provide a definitive value for the extent to which interfacial strength can be reduced in relation to numerical cohesive zone length, whilst preserving analysis accuracy, for a range of crack lengths. For the cases discussed above, a significant loss of stiffness in the elastic regime of the load-displacement curve is evident when the fully developed cohesive zone length exceeds approximately 5mm.

5. Conclusions

The present study has shown that a minimum of between 2 and 3 elements need to be present within the numerical cohesive zone for an accurate load displacement analysis to be performed under mode I, mode II and mixed mode load cases. This is necessary for an accurate representation of the numerical stress distribution within this zone at the point of

initial crack propagation.

A clear distinction has been drawn between the physical cohesive zone length, the analytical cohesive zone length and that which results from a numerical representation using interface elements. For the first time, the length of the numerical cohesive zone has been investigated in detail and compared to closed form solutions across a range of material and geometric parameters. It has been demonstrated that using a bi-linear traction-displacement curve, many current analytical formulae for cohesive zone length significantly over-predict numerical values. In addition, parameters not always included in current formulae for predicting cohesive zone length, such as specimen depth, longitudinal modulus and shear modulus, are shown to have a significant influence in slender, orthotropic materials. These findings have important implications in mesh design methods, which rely on an accurate prediction of cohesive zone length to minimise computational expense, whilst preserving the accuracy of numerical analyses. Modifications to existing formulae have been proposed for predicting cohesive zone length in standard fracture toughness tests, but they remain to be validated in more complex structural geometries. Their applicability to alternative types of traction-displacement response, such as exponential and trapezoidal forms, also requires investigation.

It has been demonstrated that although reductions in numerical interfacial strength can be used to increase the cohesive zone length and reduce the required mesh density, limits exist on the allowable magnitude of these reductions. For typical carbon epoxy composite properties, the mode I cohesive zone length is generally very short, and significant reductions in mode I interfacial strength are possible, without affecting the

accuracy of global load-displacement analyses. However, comparable reductions in mode II interfacial strength can cause excessive material softening ahead of the crack tip, due to the development of extremely long cohesive zones. This results in failure to predict the peak load at which initial crack propagation occurs in global load-displacement analyses.

Acknowledgements:

The authors would like to thank Leif Asp and Rikard Borg for their help in supplying experimental data, against which the analytical and numerical results gained in this study have been compared.

Published in Engineering Fracture Mechanics, 2008, 75(16), 4774-4792
doi:10.1016/j.compositesa.2011.12.016

Appendix A: Calculation of Elastic Modulus for Cohesive Zone Length Equations

The elastic constant *E'* that appears in equations (1) and (2) is dependent on the mode of loading, whether plane stress or plane strain conditions exist and whether the specimen can be considered as slender or infinite.

For a mode I crack in an infinite body under plane stress conditions [17]:

$$\frac{1}{E_I'} = \sqrt{\frac{b_{11}b_{33}}{2}}\sqrt{\left(\frac{b_{33}}{b_{11}}\right)^{1/2} + \frac{2b_{31}+b_{55}}{2b_{11}}} \qquad \text{(A.1)}$$

where the b_{ij} are Voigt elastic constants defined by:

$$\varepsilon_i = \sum_{j=1}^{6} b_{ij}\sigma_j\,, \qquad \text{(A.2)}$$

with $\varepsilon_1 \equiv \varepsilon_{11}, \ldots, \varepsilon_6 \equiv \varepsilon_{12}$; $\sigma_1 \equiv \sigma_{11}, \ldots, \sigma_6 \equiv \sigma_{12}$. For a specially orthotropic specimen (axes of orthotropy aligned with the axes of symmetry of the specimen), the Voigt elastic constants are related to the engineering elastic constants by:

$$b_{11} = 1/E_{11},\ b_{12} = -\nu_{12}/E_{11},\ b_{66} = 1/G_{12},$$

$$b_{22} = 1/E_{22},\ b_{23} = -\nu_{23}/E_{22},\ b_{55} = 1/G_{31}, \qquad \text{(A.3)}$$

$$b_{33} = 1/E_{33},\ b_{31} = -\nu_{31}/E_{33},\ b_{44} = 1/G_{23},$$

where E_{ii} is the Young's modulus in the x_i direction, ν_{ij} is a Poisson's ratio and G_{ij} is an engineering shear modulus. For the alignment of the specimen in figure 5, the engineering constants involved in E_I' are E_{11}, E_{33}, G_{31} and ν_{31}.

For a crack in an infinite body that is loaded in shear, the elastic constant becomes:

Published in Engineering Fracture Mechanics, 2008, 75(16), 4774-4792
doi:10.1016/j.compositesa.2011.12.016

$$\frac{1}{E'_{II}} = \sqrt{b_{11}/2}\sqrt{(b_{11}b_{33})^{1/2} + (b_{31} + b_{55}/2)} \qquad \text{(A.4)}$$

In a slender body, a different elastic constant appears. For example, in a thin plate or beam containing a mid-plane crack propagating in the x_1 direction and loaded in mode II, the elastic constant that appears in results for the cohesive zone length is the reduced Young's modulus:

$$E'_{II,slender} = \frac{E_{11}}{1 - \nu_{13}\nu_{31}} \qquad \text{(A.5)}$$

Published in Engineering Fracture Mechanics, 2008, 75(16), 4774-4792
doi:10.1016/j.compositesa.2011.12.016

Appendix B: Corrected Beam Theory Equations

(a) Mode I DCB

Considering the DCB specimen (see figure 6(a)) as two single cantilever beams, of length equal to the crack length, a, simple beam theory can be applied to give:

$$\Delta_I = \frac{2Pa^3}{3E_{11}I} \qquad \text{(B.1)}$$

where,

Δ_I = Vertical separation of cantilever beam tips

P = Point load applied to the free end of each cantilever

E_{11} = Young's Modulus of each cantilever along its length

I = Second Moment of Area of each cantilever ($=Bh^3/12$, where B and h are the specimen width and half-depth respectively, as defined in figure 5)

In order to correct the displacement for shear deformation and for local deformations that occur around the crack tip, a corrected beam theory method can be used, in which equation (B.1) becomes:

$$\Delta_I = \frac{2P(a+\chi h)^3}{3E_{11}I} \qquad \text{(B.2)}$$

where,

χ = Correction Parameter

h = cantilever depth

A value of χ can be determined both experimentally and analytically, but in this study, the analytical value presented by Reeder et al. is used [29], where:

$$\chi = \sqrt{\frac{E_{11}}{11G_{13}}\left[3 - 2\left(\frac{\Gamma}{1+\Gamma}\right)^2\right]} \qquad \text{(B.3a)}$$

and

$$\Gamma = 1.18\frac{\sqrt{E_{11}E_{22}}}{G_{13}} \qquad \text{(B.3b)}$$

The mode I strain energy release is given by [29]:

$$G_I = \frac{P^2(a + \chi h)^2}{BE_{11}I} \qquad \text{(B.4)}$$

Under a linearly increasing tip displacement, the load (P) increases until the point where $G_I = G_{IC}$ and the crack begins to propagate. The subsequent load-displacement relationship for each increment of crack extension is found by combining equations (B.2) and (B.4) with G_I set equal to G_{IC}.

(b) 3 Point ENF

The same principles apply for the 3 point ENF (see figure 6(b)), in which the displacement and mode II strain energy release rate before initial crack propagation are given by [29]:

$$\Delta_{II} = \frac{3P(a + 0.42\chi h)^3 + 2PL^3}{96E_{11}I} \qquad \text{(B.5)}$$

$$G_{II} = \frac{3(a + 0.42\chi h)^2 P^2}{64BE_{11}I} \qquad \text{(B.6)}$$

(N.B. The second moment of area, I, in equations (B.5) and (B.6) remains equal to that calculated for the DCB specimen, using half the specimen depth and the length, L, is as defined in figure 6(b).)

(c) FRMM

For the FRMM specimen (see figure 6(c)), the upper cantilever tip displacement and separate mode I and mode II strain energy release rate components are given by [30]:

$$\Delta = \frac{PN'\left[7\left(a + 0.42\chi h\right)^3 + \left(L + 2\chi h\right)^3\right]}{2Bh^3E_{11}} \tag{B.7}$$

$$G_I = \frac{3FP^2\left(a + \chi h\right)^2}{B^2h^3E_{11}} \tag{B.8}$$

$$G_{II} = \frac{9FP^2\left(a + 0.42\chi h\right)^2}{4B^2h^3E_{11}} \tag{B.9}$$

where F and N' are correction factors for large displacements and the length, L, is as defined in figure 6(c). Due to the small displacement of approximately 3mm at the point of initial crack propagation, F and N' have been assumed equal to unity for the FRMM specimen used in this study. Under a linearly increasing upper cantilever tip displacement, the analytical load, P, at which initial crack propagation occurs was calculated using the power law failure criterion given by equation (5), with $\alpha = 1$.

References

[1] Mi Y; Crisfield,MA; Davies,GAO Hellweg H.-B. Progressive Delamination Using Interface Elements. Journal of Composite Materials 1998;32:1246-1272.

[2] Petrossian,Z; Wisnom,MR. Prediction of delamination initiation and growth from discontinuous plies using interface elements. Composites Part A: Applied Science and Manufacturing 1998;29A:503-515.

[3] Chen,J; Crisfield,M; Kinloch,AJ; Busso,EP; Matthews,FL; Qiu,Y. Predicting Progressive Delamination of Composite Material Specimens via Interface Elements. Mechanics of Composite Materials and Structures 1999;6:301-317.

[4] Crisfield,MA; Alfano,G. Finite element interface models for the delamination analysis of laminated composites: mechanical and computational issues. International journal for numerical methods in engineering 2000;50:1701-1736.

[5] Camanho,PP; Davila,CG; De Moura,MF. Numerical Simulation of Mixed-mode Progressive Delamination in Composite Materials. Journal of Composite Materials 2003;37:1415-1424.

[6] Pinho,ST; Ianucci,L; Robinson,P. Formulation and implementation of decohesion elements in an explicit finite element code. Composites Part A: Applied Science and Manufacturing 2006;37:778-789.

[7] Jiang,WG; Hallett,SR; Green,BG; Wisnom,MR. A concise interface constitutive law for analysis of delamination and splitting in composite materials and its

application to scaled notched tensile specimens. International journal for numerical methods in engineering 2007;69:1982-1995

[8] Camanho,PP; Davila,CG; Pinho,ST. Fracture Analysis of Composite Co-cured Structural Joints Using Decohesion Elements. Fatigue Fract Engng Mater Struct, 2003;27:745-757.

[9] Blackman,BRK; Hadavinia,H; Kinloch,AJ; Williams,JG. The use of a cohesive zone model to study the fracture of fibre composites and adhesively-bonded joints. International Journal of Fracture 2003;119:25-46.

[10] Li,S; Thouless,MD; Waas,AM; Schroeder,JA; Zavattieri,PD. Mixed-mode cohesive-zone models for fracture of an adhesively bonded polymer-matrix composite. Engineering Fracture Mechanics 2006;73:64-78.

[11] Goyal,VK; Johnson,ER; Goyal,VK. Predictive strength-fracture model for composite bonded joints. Composite Structures 2008;82:434-446.

[12] Cox,B; Yang,Q. Cohesive Models for damage evolution in laminated composites. International Journal of Fracture 2005;133:107-137.

[13] Shet,C; Chandra,N. Effect of the Shape of traction-displacement cohesive zone curves on the fracture response. Mechanics of Advanced Materials and Structures 2004;11:249-275.

[14] Turon,A; Davila,CG; Camanho,PP; Costa,J. An engineering solution for mesh size effects in the simulation of delamination using cohesive zone models. Engineering Fracture Mechanics 2007;74:1665-1682

[15] Turon,A; Costa,J; Camanho,PP; Davila,CG. Simulation of delamination in composites under high-cycle fatigue. Composites Part A: Applied Science and Manufacturing 2007;38:2270-2282.

[16] Hillerborg A; Modeer, M, Petersson PE. Analysis of crack formation and growth in concrete by means of fracture mechanics and finite elements. Cement and Concrete Research 1976;6:773-782.

[17] Yang,QD; Cox,BN; Nalla,RK; Ritchie,RO. Fracture length scales in human cortical bone: The necessity of nonlinear fracture models. Biomaterials 2006;27:2095-2113.

[18] Planas J; Elices M. Nonlinear fracture of cohesive materials. International Journal of Fracture 1991;51:139-157.

[19] Smith, E. The effect of the stress-relative displacement law on failure predictions using the cohesive zone model. International Journal of Fracture 1999;99:41-51

[20] Williams,JG; Hadavinia,H. Analytical solutions for cohesive zone models. Journal of the Mechanics and Physics of Solids 2002;50:809-825

[21] Bao,G; Suo,Z. Remarks on crack-bridging concepts. Applied Mechanics Reviews 1992;24:355-366.

[22] Massabo,R; Cox,BN. Concepts for bridged mode II delamination cracks. Journal of the Mechanics and Physics of Solids 1999;47:1265-1300.

[23] Barua,A; Bose,K. On the Optimum Choices of Cohesive-Zone Parameters Describing Initiation and Propagation of Cracks. ECCOMAS Thematic Conference on Mechanical Response of Composites, Porto, Portugal, 12-14 September 2007.

[24] Hallett,SR; Wisnom,MR. Modelling and experimental investigation of progressive damage in notched composites, 17th American Society for Composites Technical Conference, West Lafayette, 2002

[25] Asp,LE; Sjogren,A; Greenhalgh,ES. Delamination Growth and Thresholds in a Carbon/Epoxy Composite Under Fatigue Loading. Journal of Composites Technology and Research 2001;23:55-68.

[26] Borg,R; Nilsson,L; Simonsson,K. Modelling of delamination using a discretized cohesive zone and damage formulation. Composites Science and Technology 2002;62:1299-1314.

[27] Borg,R; Nilsson,L; Simonsson,K. Simulating DCB, ENF and MMB experiments using shell elements and a cohesive zone model. Composites Science and Technology 2004;64:269-278.

[28] Robinson,P; Galvanetto,U; Tumino,D; Belluci,G. Numerical simulation of fatigue-driven delamination using interface elements. International Journal for Numerical Methods in Engineering 2004;63:1824-1848.

[29] Reeder,JR; Demarco,K; Whitley,KS. The use of doubler reinforcement in delamination toughness testing. Composites Part A: Applied Science and Manufacturing 2004;35:1337-1344.

[30] Kinloch,AJ; Wang,Y; Williams,JG; Yayla,P. The Mixed-Mode Delamination of Fibre Composite Materials. Composites Science and Technology 1993;47: 225-237.

Published in Engineering Fracture Mechanics, 2008, 75(16), 4774-4792
doi:10.1016/j.compositesa.2011.12.016

Figures

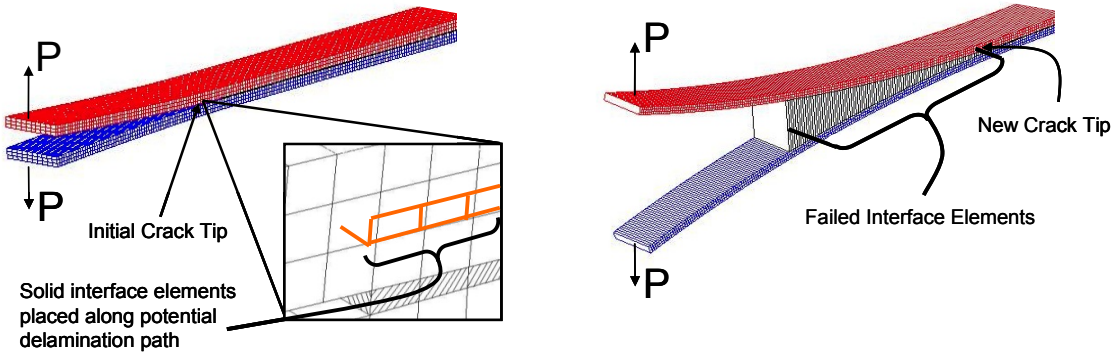

Figure 1: Interface element analysis of delamination in a Double Cantilever Beam

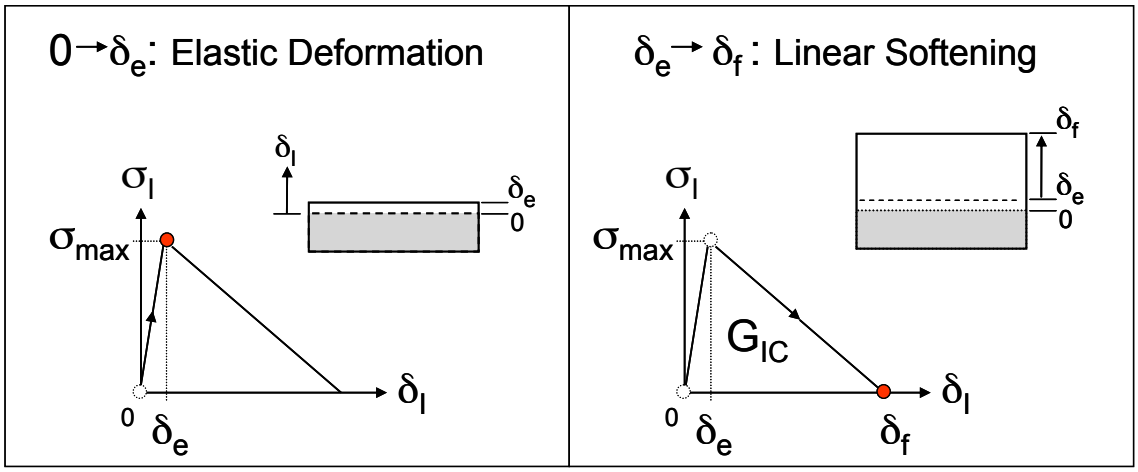

Figure 2: Bi-linear traction-displacement response

Published in Engineering Fracture Mechanics, 2008, 75(16), 4774-4792
doi:10.1016/j.compositesa.2011.12.016

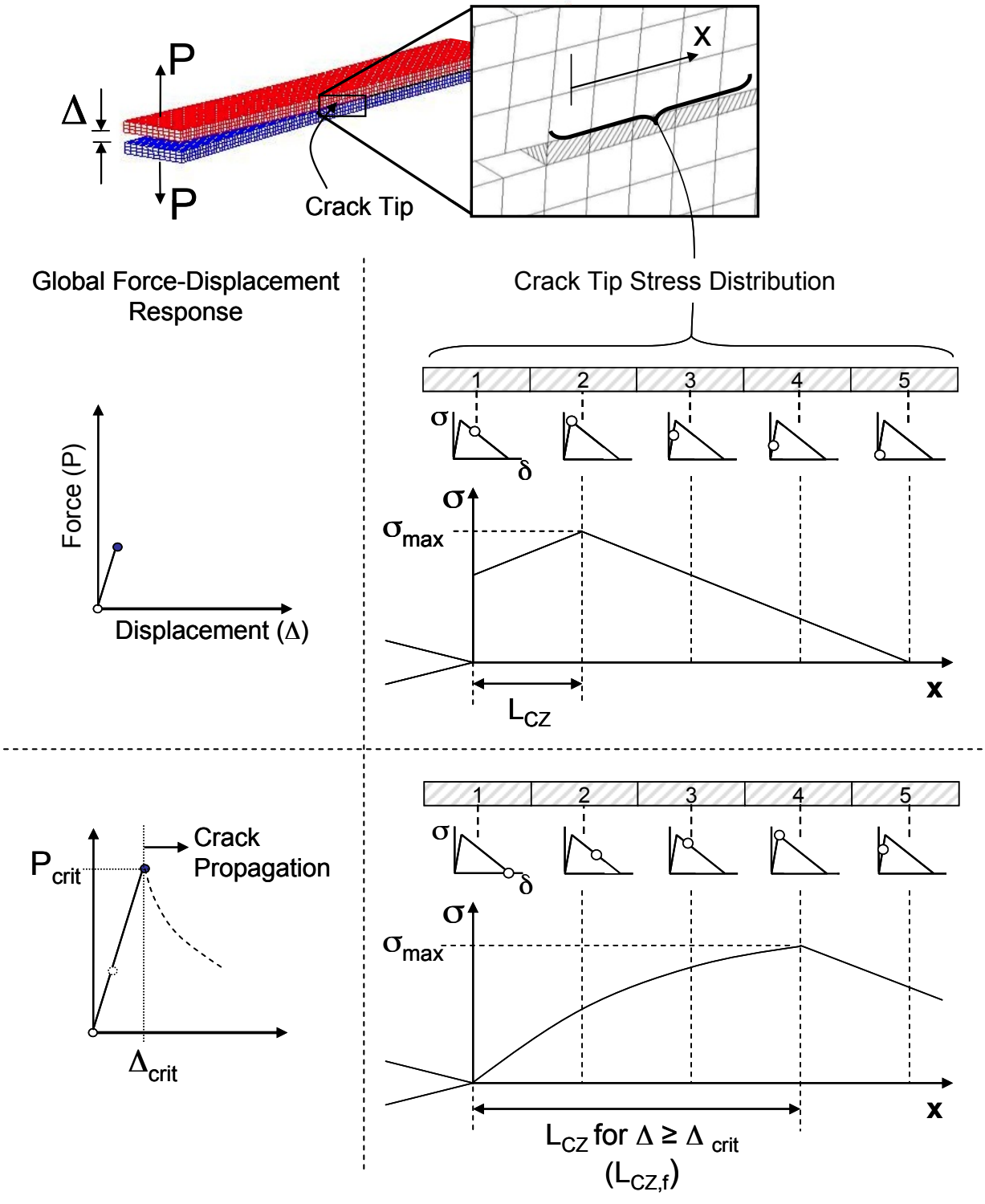

Figure 3: Development of the numerical cohesive zone

Published in Engineering Fracture Mechanics, 2008, 75(16), 4774-4792
doi:10.1016/j.compositesa.2011.12.016

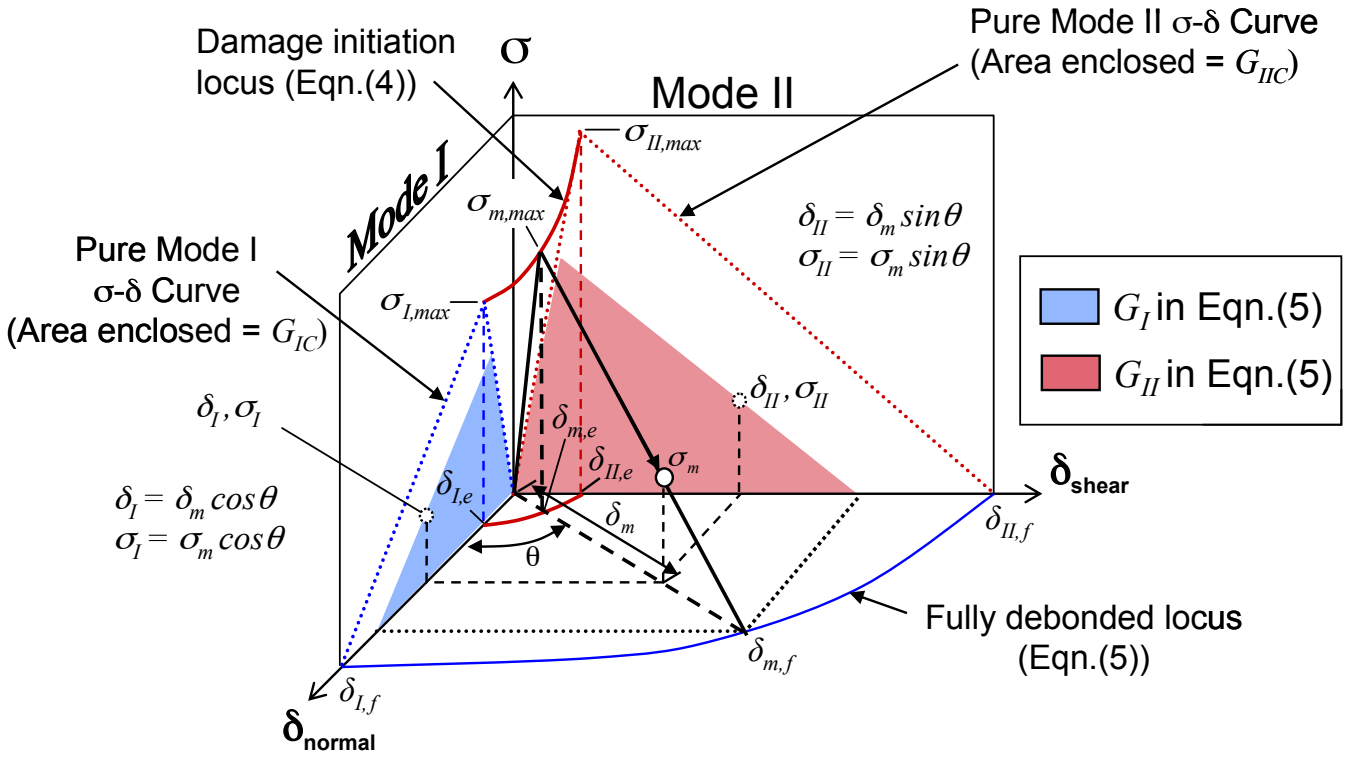

Figure 4: Bilinear mixed mode softening law

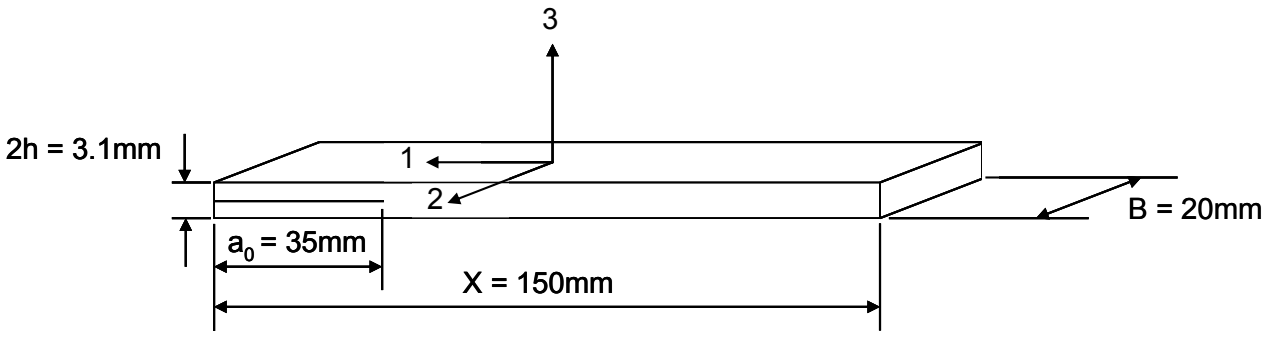

Figure 5: Baseline Specimen Geometry

Published in Engineering Fracture Mechanics, 2008, 75(16), 4774-4792
doi:10.1016/j.compositesa.2011.12.016

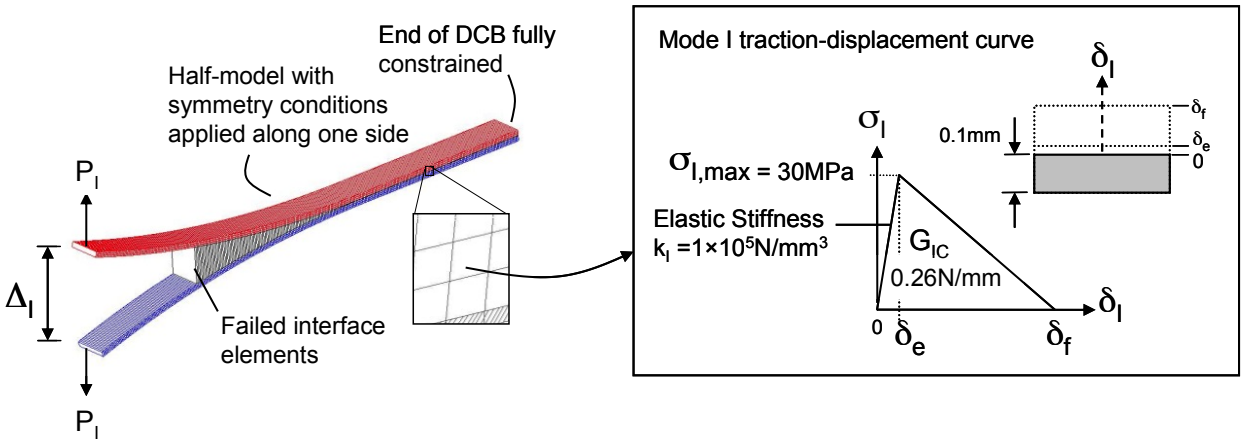

(a) Mode I DCB

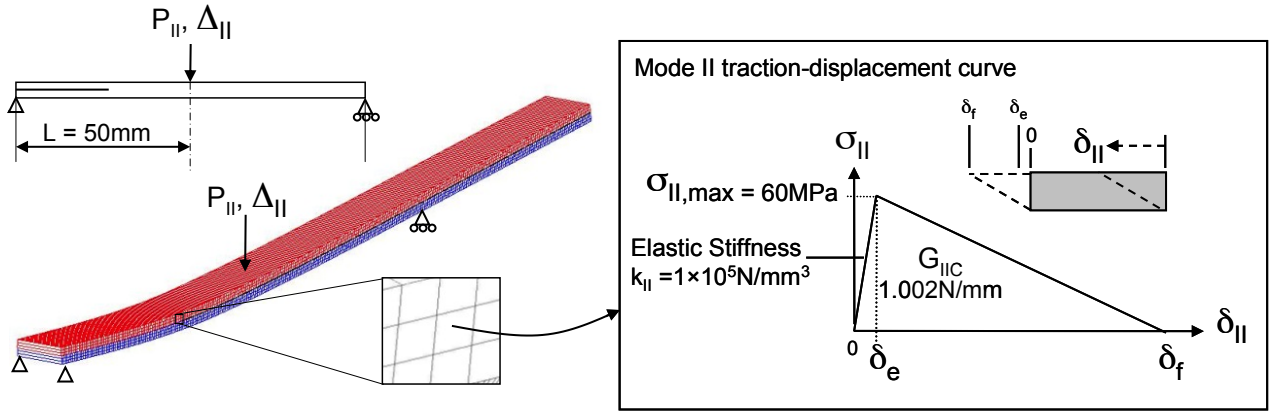

(b) Mode II 3ENF

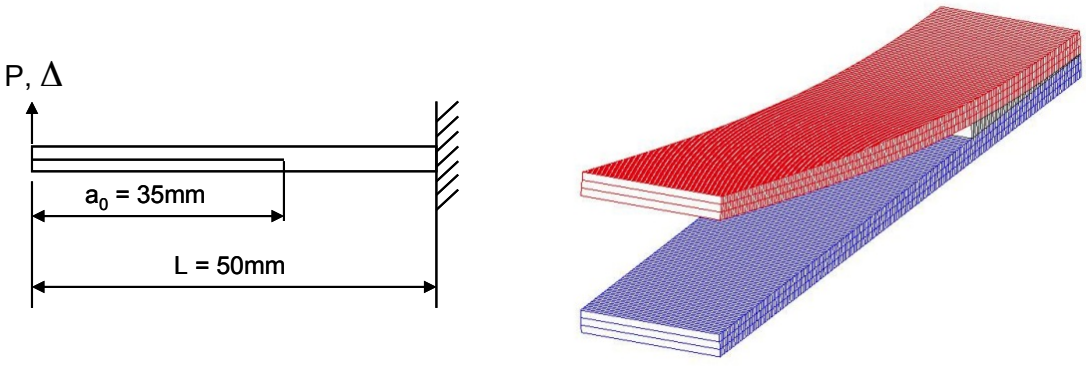

(c) FRMM

Figure 6: Finite element models for the benchmark load cases

Published in Engineering Fracture Mechanics, 2008, 75(16), 4774-4792
doi:10.1016/j.compositesa.2011.12.016

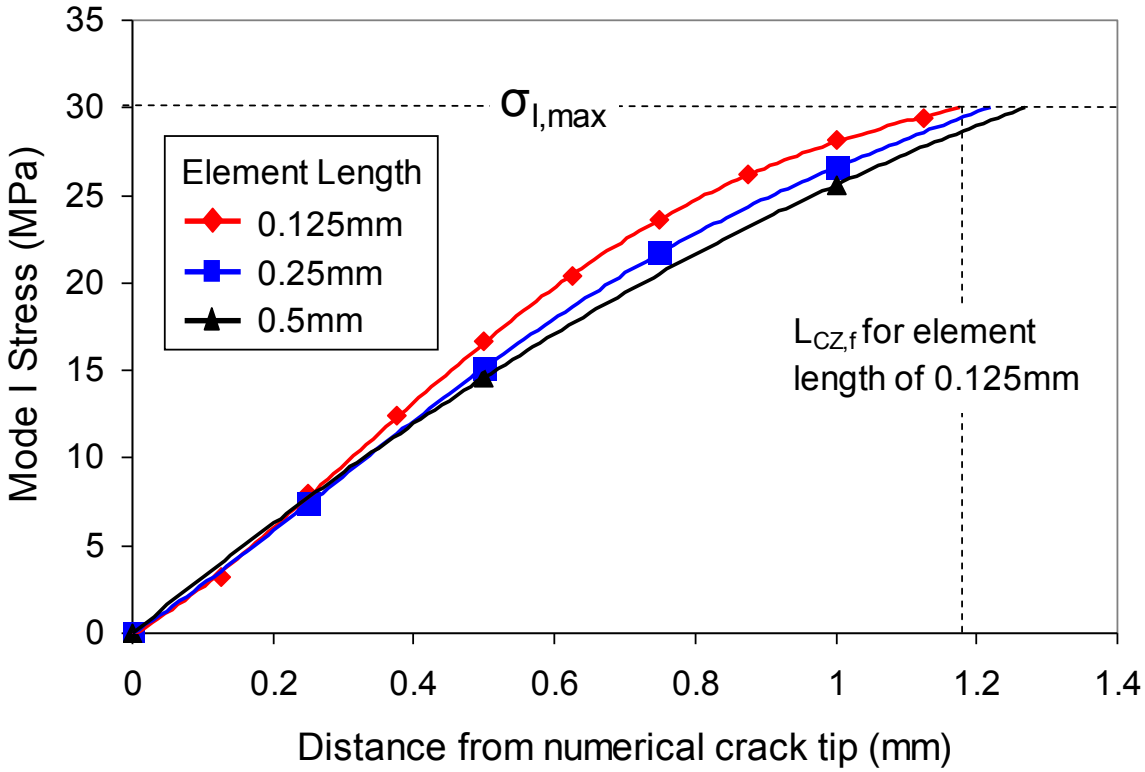

Figure 7: Cohesive Zone Stress Distribution for DCB model at point of first element failure

Published in Engineering Fracture Mechanics, 2008, 75(16), 4774-4792
doi:10.1016/j.compositesa.2011.12.016

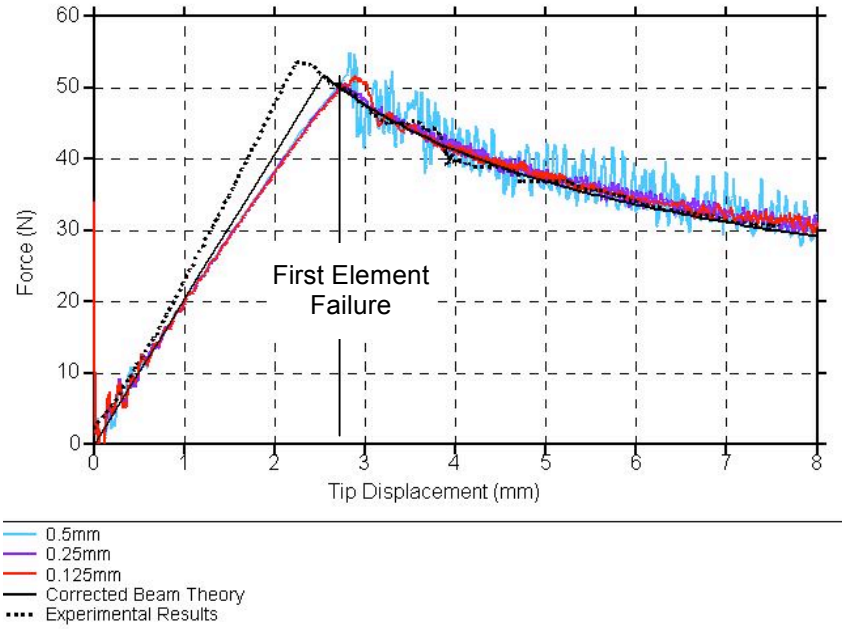

(a) **Minimum of two interface elements within cohesive zone at point of first element failure**

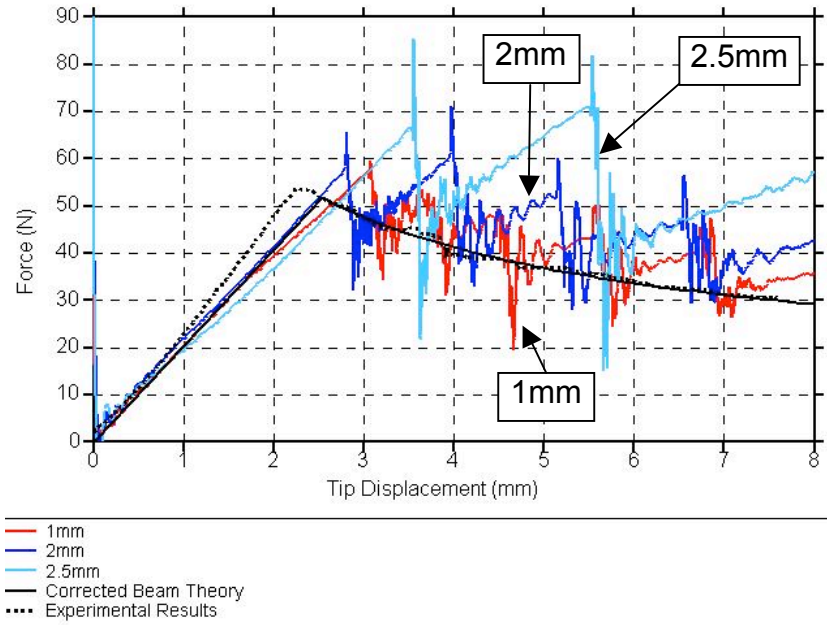

(b) **Less than 2 elements within cohesive zone at point of first element failure**

Figure 8: DCB Load-Displacement Curves in relation to the number of interface elements within the numerical cohesive zone

Published in Engineering Fracture Mechanics, 2008, 75(16), 4774-4792
doi:10.1016/j.compositesa.2011.12.016

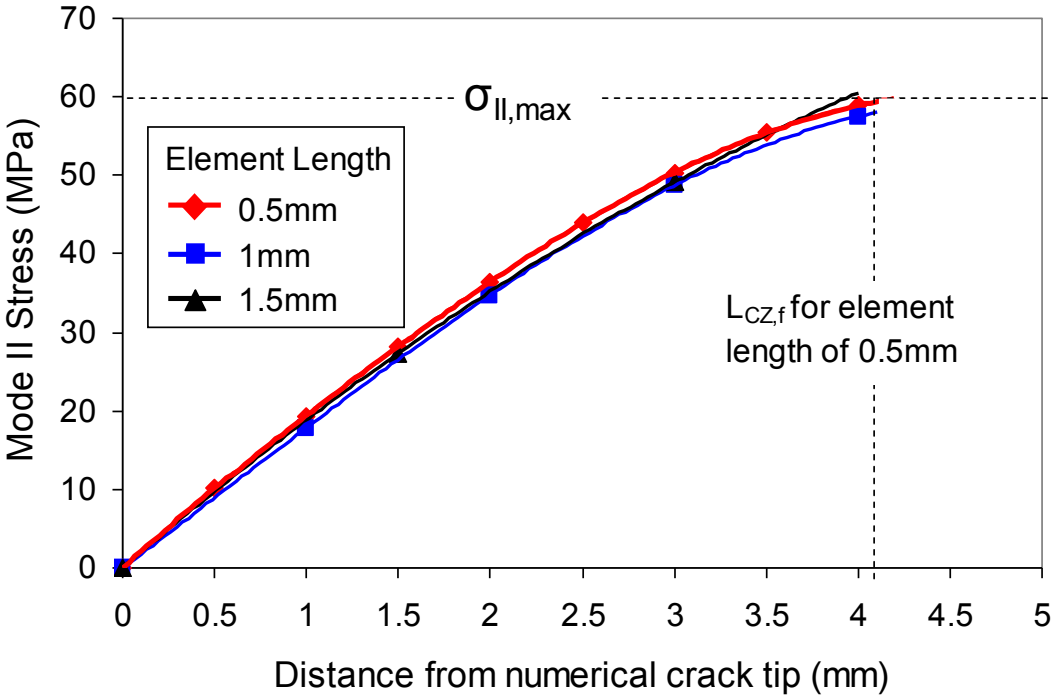

Figure 9: Cohesive Zone Stress Distribution for 3ENF model at point of first element failure

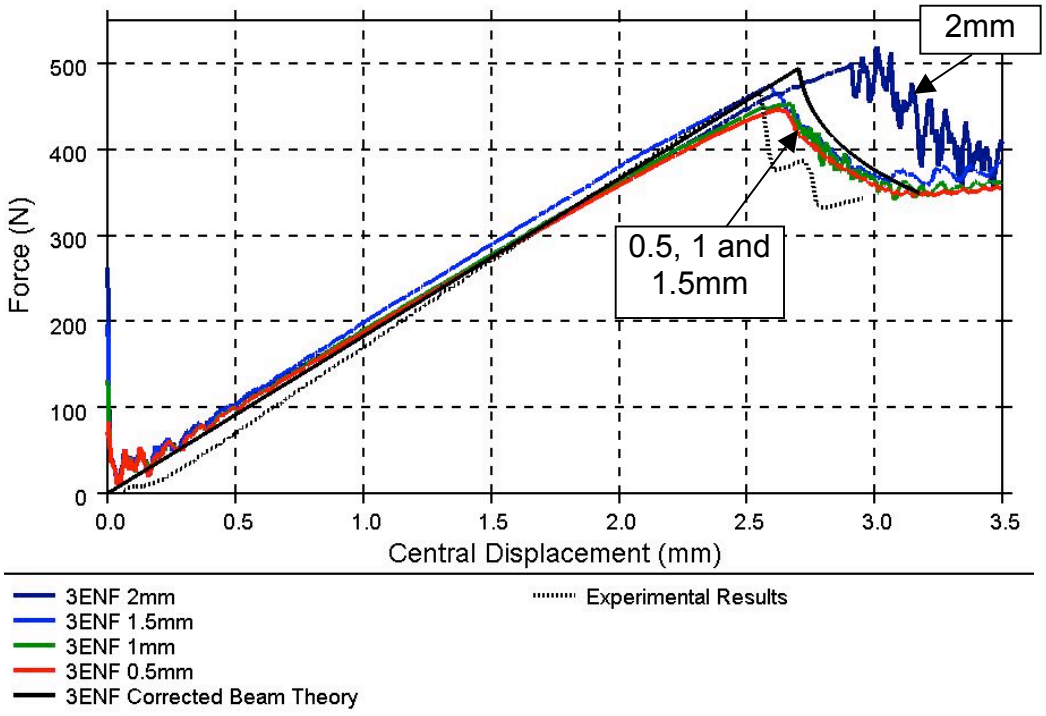

Figure 10: 3ENF Load-Displacement Curves for a range of element lengths

Published in Engineering Fracture Mechanics, 2008, 75(16), 4774-4792
doi:10.1016/j.compositesa.2011.12.016

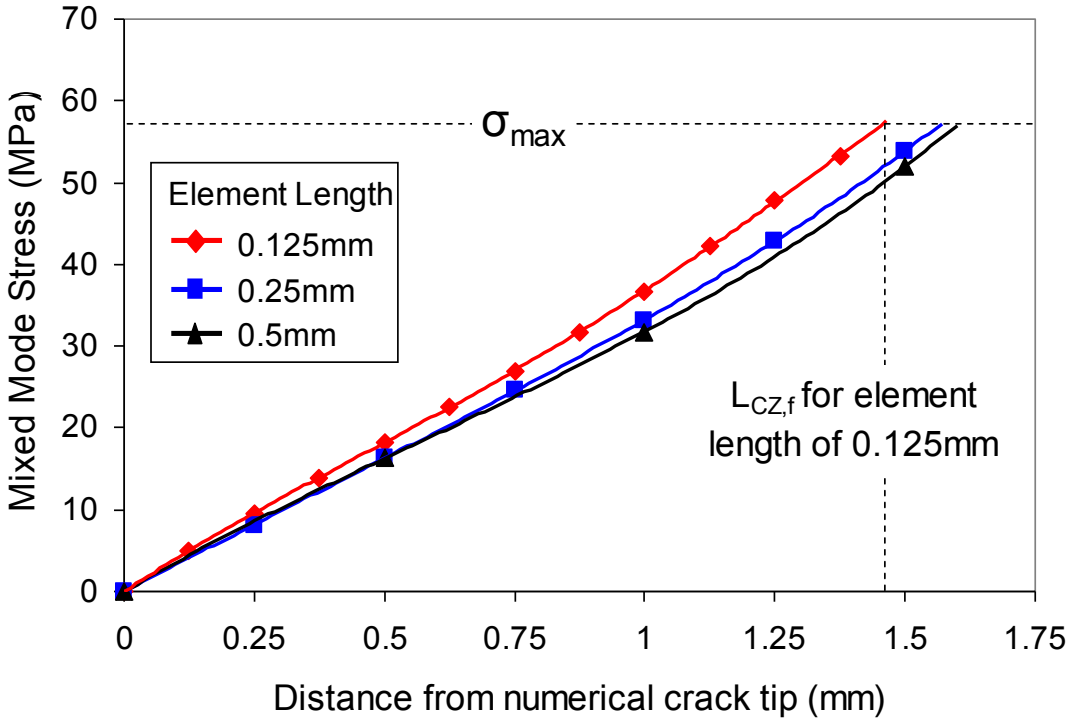

Figure 11: Cohesive Zone Stress Distribution for FRMM model at point of first element failure

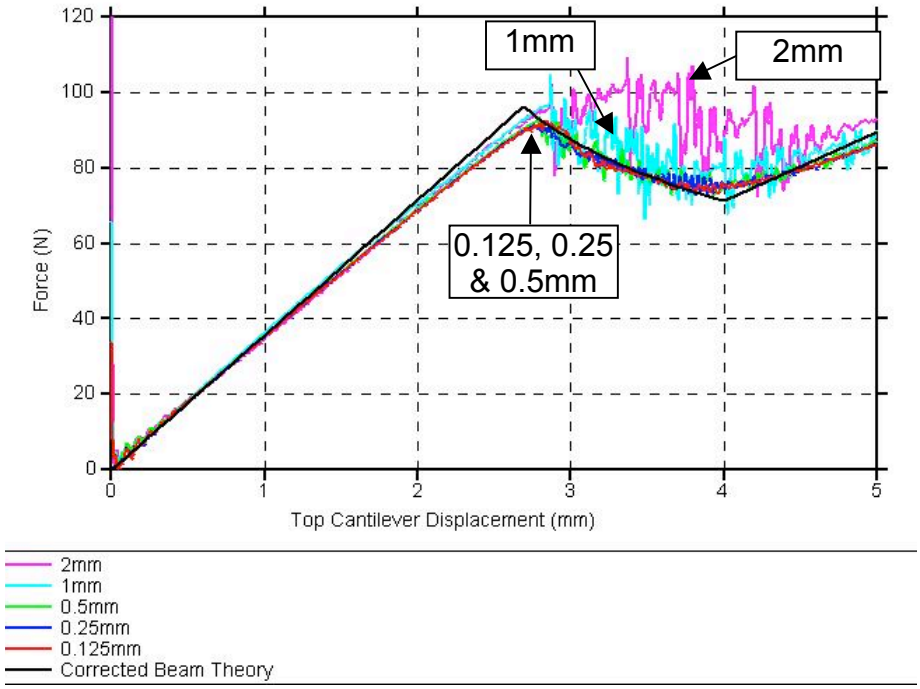

Figure 12: FRMM Load-Displacement Curves for a range of element lengths

Published in Engineering Fracture Mechanics, 2008, 75(16), 4774-4792
doi:10.1016/j.compositesa.2011.12.016

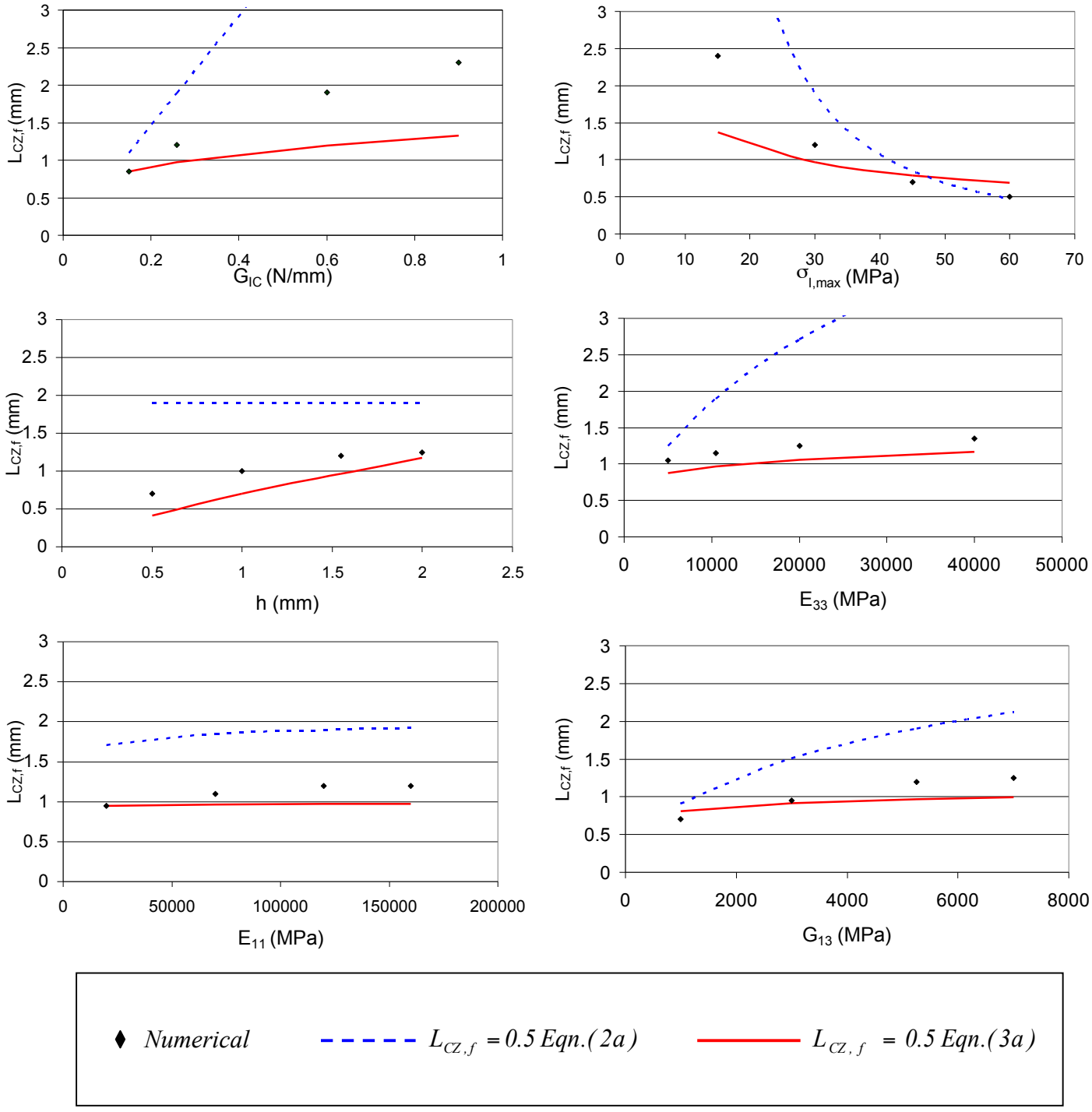

Figure 13: Effect of material properties and depth on mode I cohesive zone length for the HTA6376/C benchmark DCB model

Published in Engineering Fracture Mechanics, 2008, 75(16), 4774-4792
doi:10.1016/j.compositesa.2011.12.016

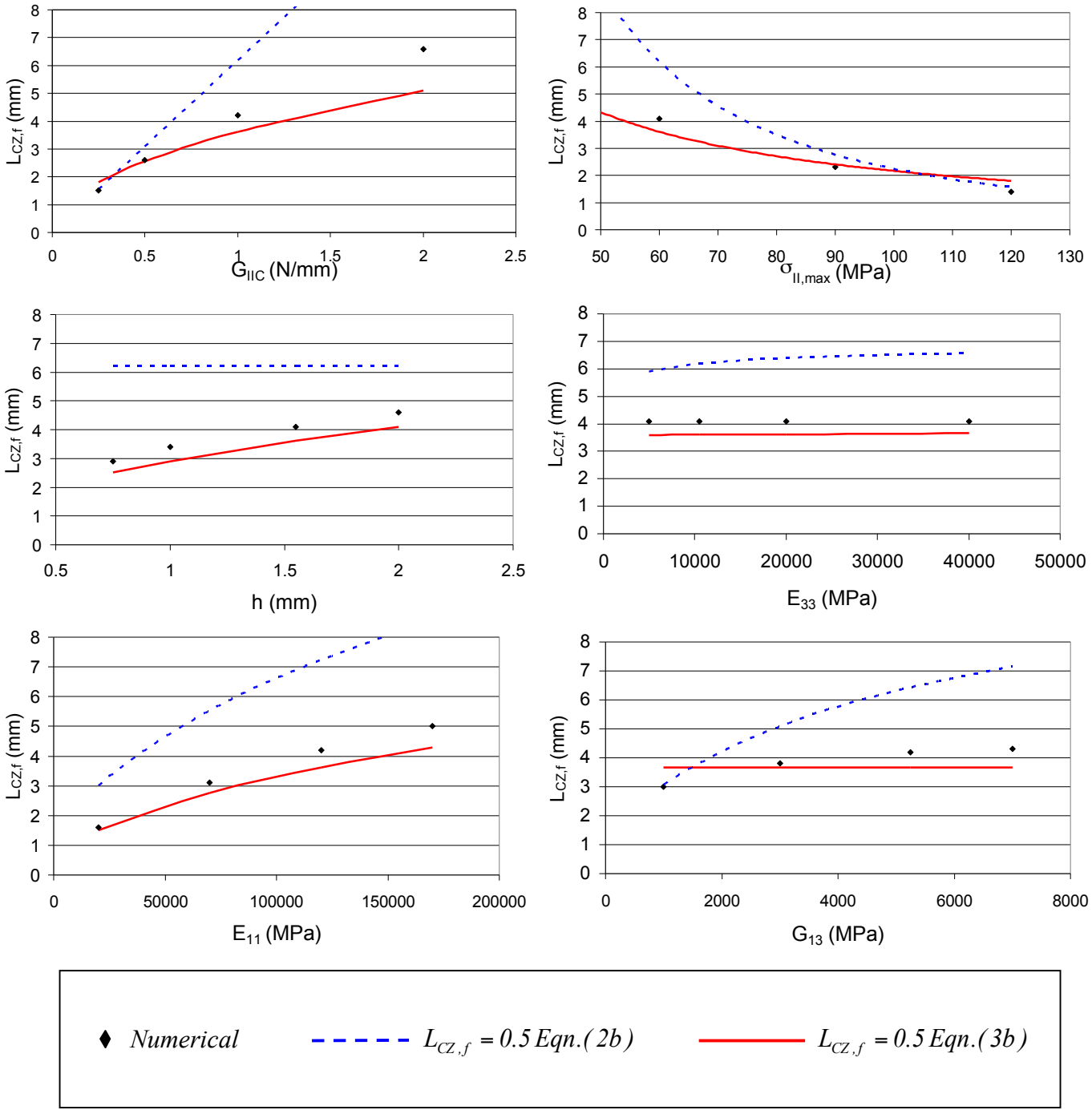

Figure 14: Effect of material properties and depth on mode II cohesive zone length for the HTA/6376C benchmark 3ENF model

Published in Engineering Fracture Mechanics, 2008, 75(16), 4774-4792
doi:10.1016/j.compositesa.2011.12.016

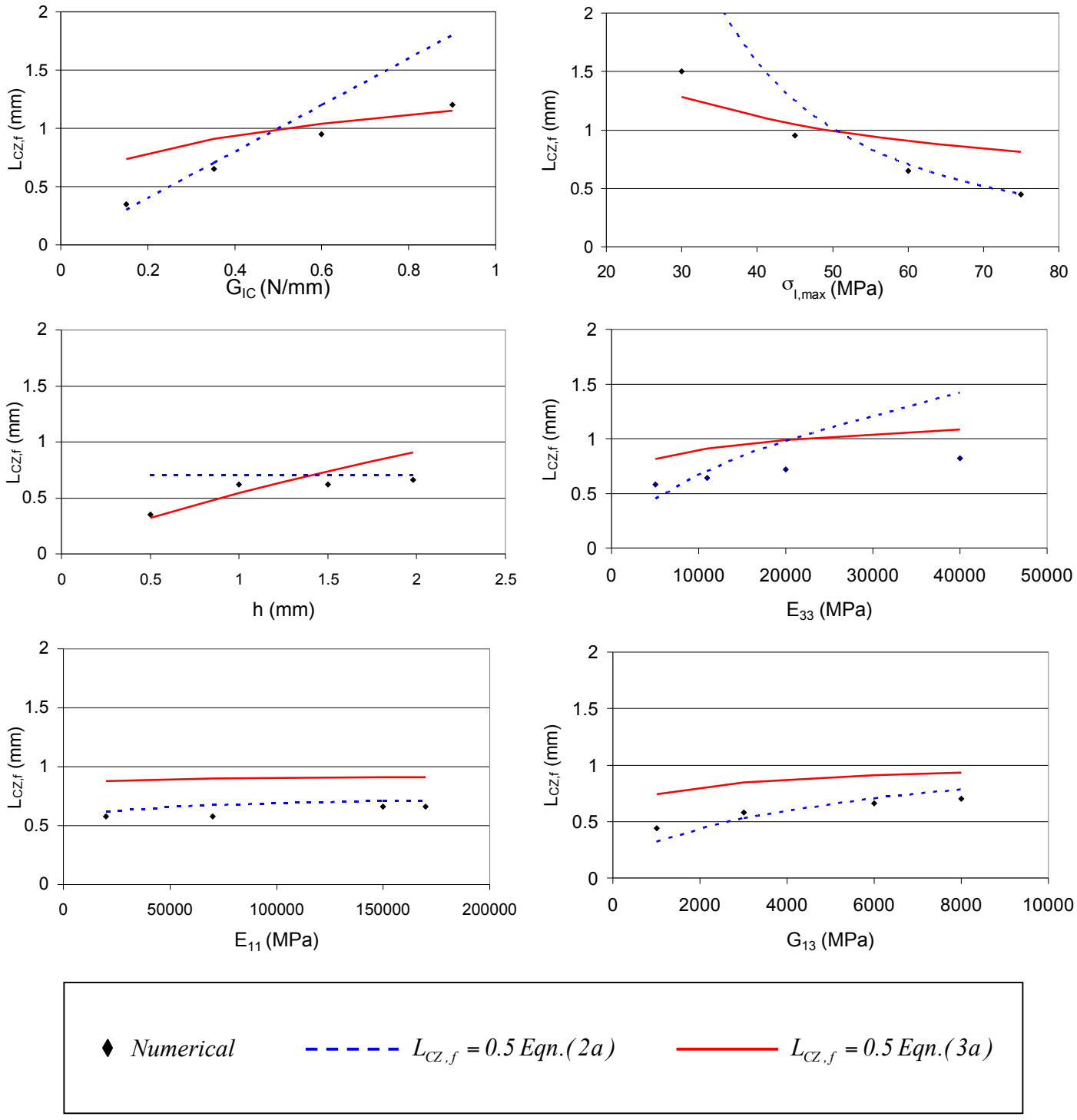

Figure 15: Effect of material properties and depth on mode I cohesive zone length for a T300/977-2 DCB model

Published in Engineering Fracture Mechanics, 2008, 75(16), 4774-4792
doi:10.1016/j.compositesa.2011.12.016

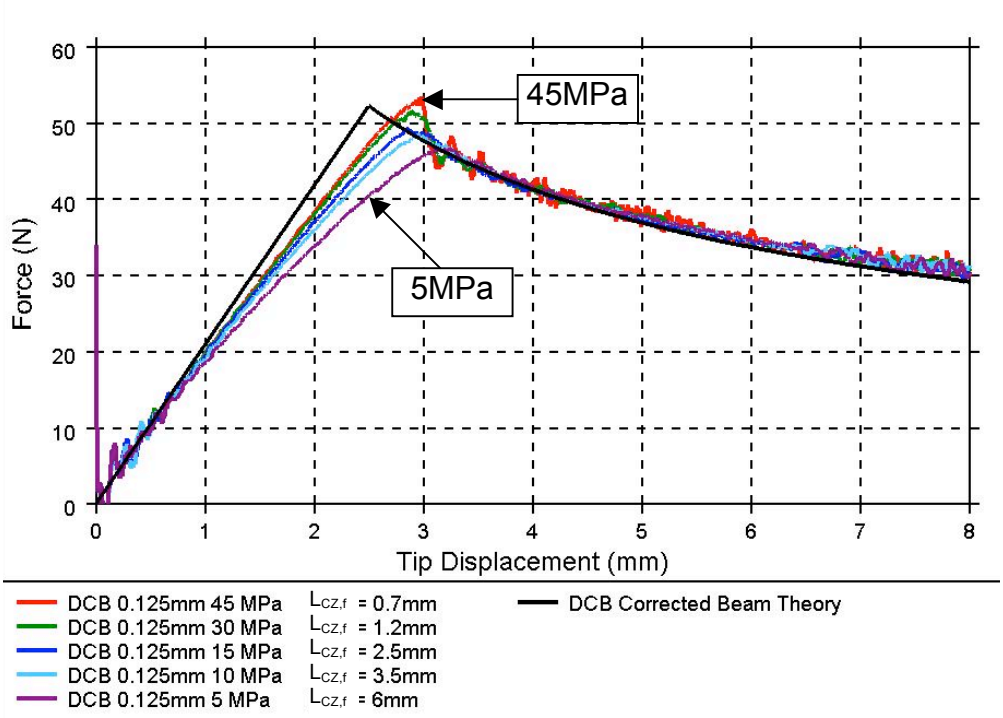

(a) Fine mesh (0.125mm element length)

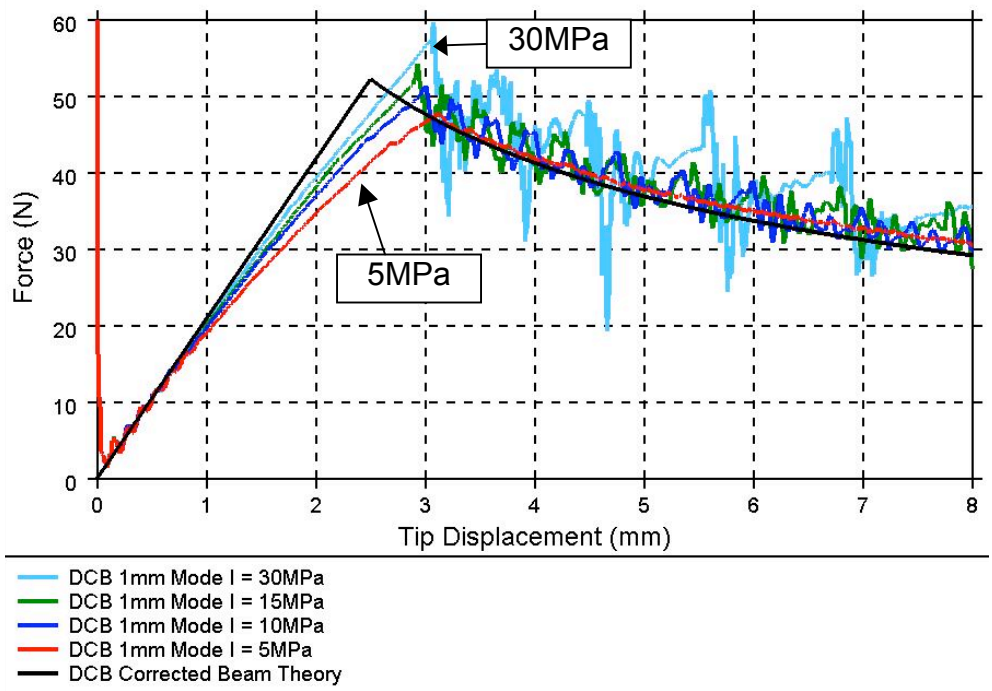

(b) Coarse mesh (1mm element length)

Figure 16: Effect of numerical interfacial strength variation on mode I DCB model (HTA/6376C)

Published in Engineering Fracture Mechanics, 2008, 75(16), 4774-4792
doi:10.1016/j.compositesa.2011.12.016

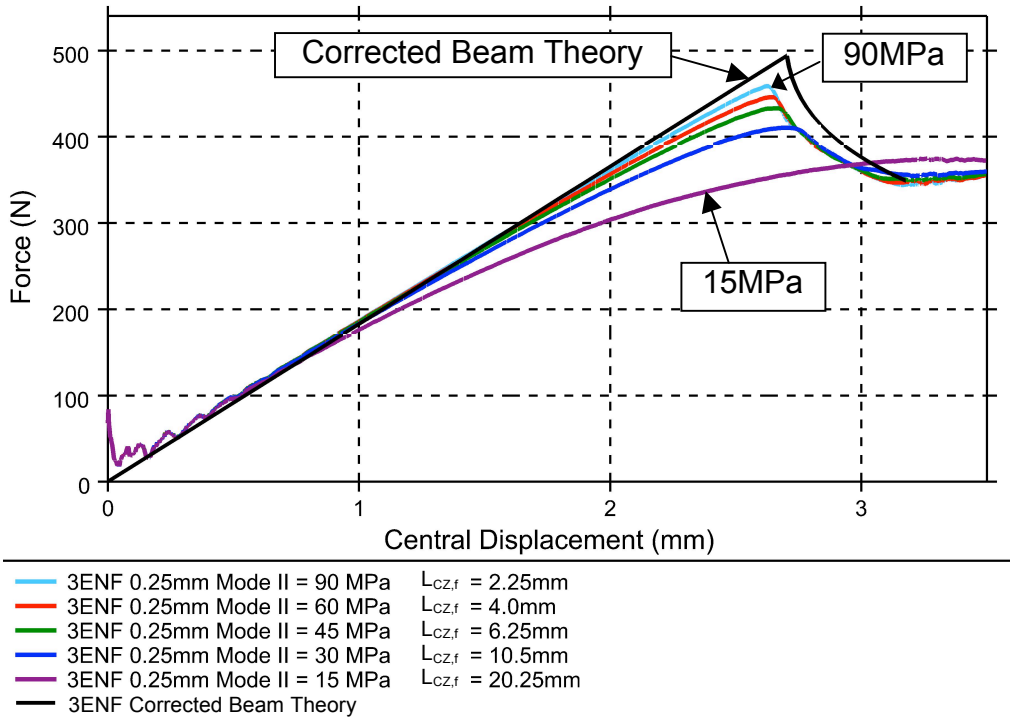

(a) Fine mesh (0.25mm element length)

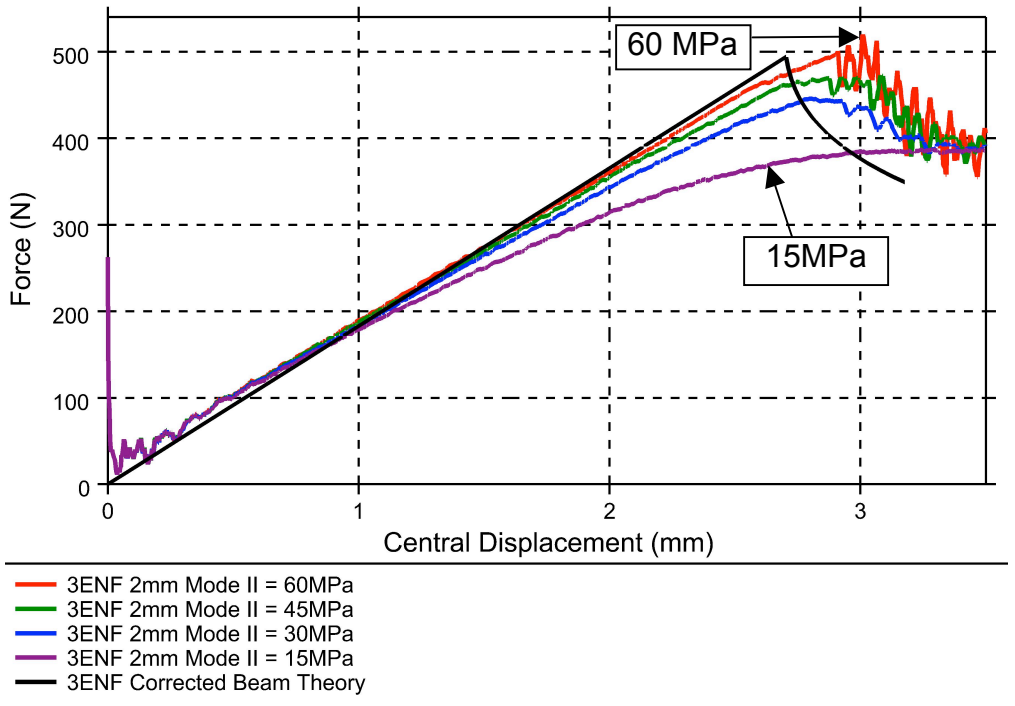

(b) Coarse mesh (2mm element length)

Figure 17: Effect of numerical interfacial strength variation on mode II 3ENF model (HTA/6376C)

Published in Engineering Fracture Mechanics, 2008, 75(16), 4774-4792
doi:10.1016/j.compositesa.2011.12.016

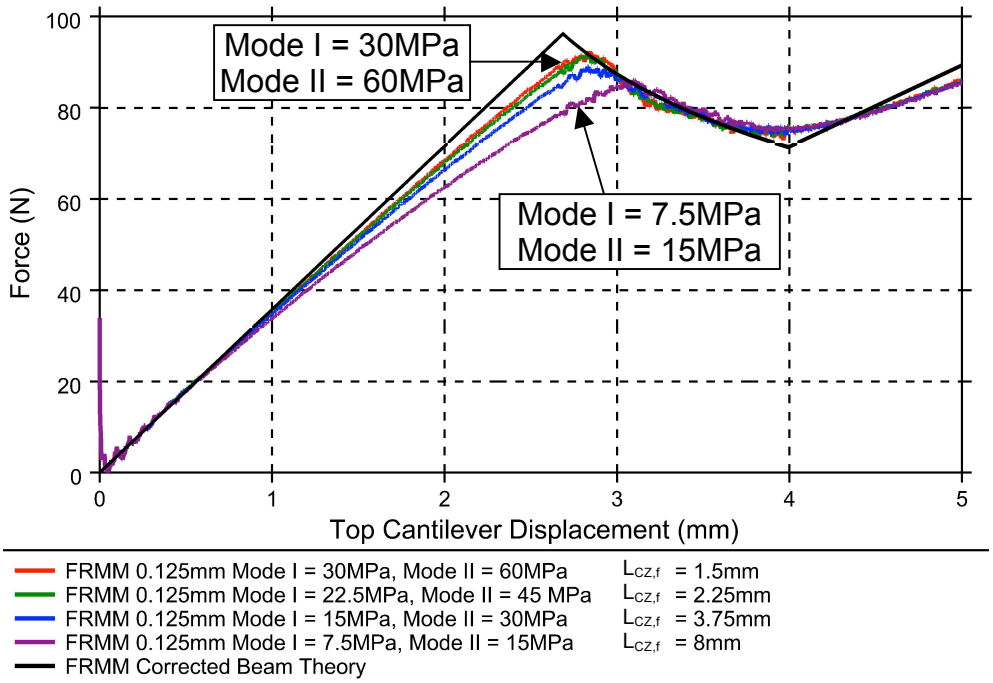

(a) Fine mesh (0.125mm element length)

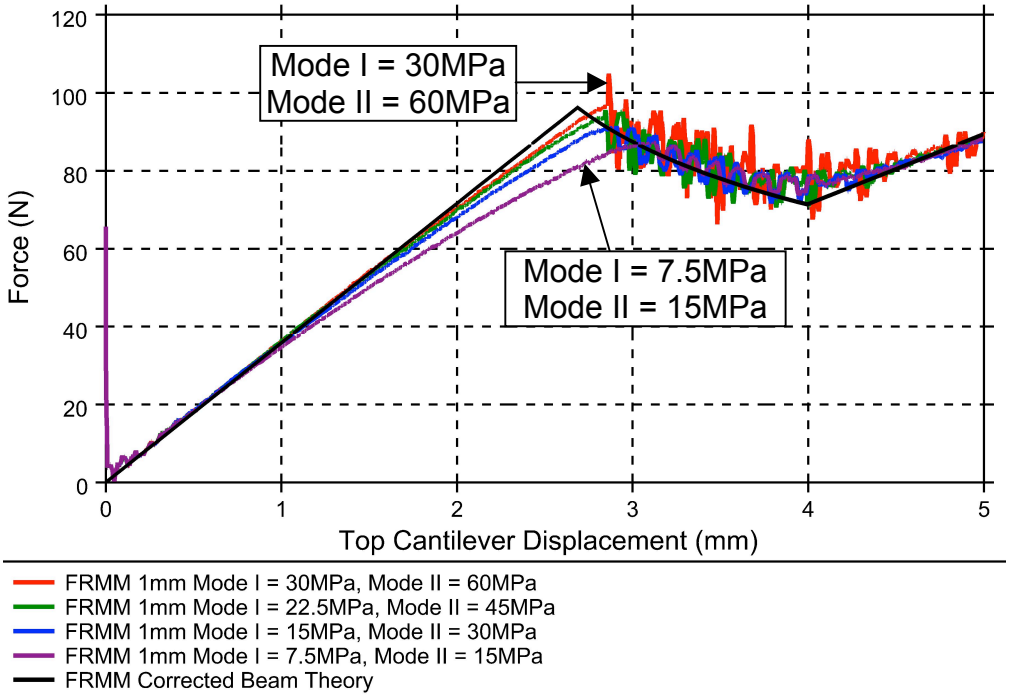

(b): Coarse mesh (1mm element length)

Figure 18: Effect of numerical interfacial strength variation on FRMM model (HTA/6376C)

Published in Engineering Fracture Mechanics, 2008, 75(16), 4774-4792
doi:10.1016/j.compositesa.2011.12.016

Table 1: Material Properties for HTA6376/C

Laminate Properties		**Interfacial Properties**	
E_{11} (MPa)	120,000	G_{IC} (N/mm)	0.26
$E_{22} = E_{33}$ (MPa)	10,500	G_{IIC} (N/mm)	1.002
$G_{12} = G_{13}$ (MPa)	5,250	$\sigma_{I,max}$ (MPa)	30
G_{23} (GPa)	3,480	$\sigma_{II,max}$ (MPa)	60
$v_{12} = v_{13}$	0.3	K_I (N/mm^3)	1×10^5
v_{23}	0.51	K_{II} (N/mm^3)	1×10^5

Table 2: Material and geometric properties for T300/977-2 DCB model

Laminate Properties		**Interfacial Properties**	
E_{11} (MPa)	150,000	G_{IC} (N/mm)	0.352
$E_{22} = E_{33}$ (MPa)	11,000	$\sigma_{I,max}$ (MPa)	60
$G_{12} = G_{13}$ (MPa)	6,000	G_{IIC} (N/mm)	1.002
G_{23} (MPa)	3,700	$\sigma_{II,max}$ (MPa)	60
$v_{12} = v_{13}$	0.3	K_I (N/mm^3)	1×10^5
v_{23}	0.51	K_{II} (N/mm^3)	1×10^5
Geometric Properties			
X (mm)	150	h (mm)	1.98
a_0 (mm)	55	B (mm)	20

(N.B. The poisson ratios (v_{12},v_{13},v_{23}), mode II interfacial properties (G_{IIC}, $\sigma_{II,max}$, K_{II}) and mode I interfacial stiffness (K_I) shown in table 2 are identical to those applied for the HTA/6376C specimen. All other properties are consistent with those shown in reference [14] for a T300/977-2 mode I DCB specimen.)